PART SCALE SIMULATION OF HEAT AFFECTED ZONES FOR PARAMETER OPTIMIZATION IN A MICROSCALE SELECTIVE LASER SINTERING SYSTEM

J. Grose*, A. Liao*, F. Tasnim*, C. S. Foong†, and M. A. Cullinan*

*Department of Mechanical Engineering, The University of Texas at Austin, Austin, TX 78712
†NXP Semiconductors, Austin, TX 78735

Abstract

The Microscale Selective Laser Sintering (μ-SLS) system can produce feature sizes on the order of a single micrometer, far smaller than existing metal additive technologies. Despite this advantage, there are challenges in producing reliable small-scale parts due to unwanted heat transfer in the nanoparticle bed. To address this issue, a multiscale Finite Element thermal model has been developed to predict the temperature changes that occur during sintering within the particle bed. Nanoscale particle models are used to quantify material property changes experienced by particle groups that undergo laser sintering. This work processes the property relationships developed by the particle models and integrates comprehensive property functions into the part-scale model to capture the nuanced thermal evolution that occurs during sintering. The multiscale model predicts the extent of heat spread and part formation during sintering to optimize input laser parameters, reduce unwanted heat spread, and improve the minimum feature resolution of printable parts.

1. Introduction

1.1 μ-SLS Background

Additive Manufacturing (AM) technologies that are currently available for advanced manufacturing applications are restricted by minimum producible feature resolutions on the order of 100 micrometers. This limits the applicability of these technologies to many critical manufacturing domains such as advanced semiconductor packaging [1, 2]. The μ-SLS system, developed at the University of Texas at Austin, resolves this limitation by facilitating the production of copper and silver structures with single micrometer feature resolutions [3-6]. The μ-SLS machine is derived from Selective Laser Sintering (SLS), an AM process where laser energy is applied to a powdered substrate in select regions to drive a melting and solidification process that forms a single layer part. This process is repeated layer-by-layer to form complex 3D structures [7]. The μ-SLS system modifies the base SLS process by replacing the macroscale powders with silver and copper nanoparticle inks. These nanoparticles have average diameters on the order of 100 nanometers, and therefor experience a solid-state diffusion process (below the melting temperature) when exposed to laser heating. With custom physics-based modeling strategies, the μ-SLS system can be optimized to take full advantage of the small particle sizes and produce parts with the desired minimum feature resolutions. The sintering process present in the μ-SLS system is fundamentally a thermally driven process, therefore thermal modeling techniques are required to capture the underlying physical processes present in the system.

The flow of heat through a solid body is governed by the heat conduction equation shown in Equation 1:

$$\rho c_p \frac{\partial T}{\partial t} = \nabla \cdot (\mathrm{k}\nabla \mathrm{T}) + Q''' \qquad (1)$$

where k, ρ, c_p, and T represent the thermal conductivity, density, specific heat, and temperature of the solid object under consideration. The terms on the right side of the equality represent the second order spatial temperature gradient in the solid body in each of the three Cartesian coordinate directions as well as the volumetric heat generation within the body. The terms on the left side of the equation represent the transient thermal response of the system. Solutions to the heat equation provide detailed information on the temperature distribution throughout an object. For most real problems, simple analytical solutions to the heat equation are not obtainable. Instead, approximations to these solutions are needed to provide accurate temperature information within a physical domain. The primary method used to determine these approximate solutions to the heat equation is through Finite Element (FE) modeling. A bed-scale FE thermal model is developed in this work to predict heat spread and temperature evolution in the μ-SLS particle bed. These thermal predictions can then be used to predict and minimize the formation of unwanted heat affected zones (regions of sintered nanoparticles that extend beyond the target part shape).

Most existing part-scale thermal models for laser-based AM technologies focus on selective laser melting and model the phase change processes that occur in these systems. Additional models analyze processes related to metal nanoparticles using functional representations for critical material properties.

1.2 Selective Laser Melting: Thermal Simulations with Phase Change

Foroozmehr, Badrossamay and Foroozmehr used ANSYS APDL to simulate a moving gaussian laser across a stainless steel 316L powder bed and determine the size of the resulting melt pool. They estimate the initial powdered thermal conductivity as 1% of the bulk value. The phase change experienced by metal particles during melting and solidification is modeled using phase and temperature dependent material properties [8]. Similarly, Bruna-Rosso, Demir and Previtali use temperature and phase dependent material properties and a moving heat source to predict melt pool geometries. This model employs Goldak's double ellipsoidal heat source model to simulate the laser heat source [9]. Huang et al., Lee and Yun, and Fu and Guo performed similar modeling work using $TiAl_6V_4$ powder [10, 11, 12]. Huang compared the impact of modifying scan speed and laser power on process capability and determined that increasing laser power was preferred over a reduction in scan speed. Lee simulated the full SLM printing of a supported cantilever structure using ABAQUS. Liu et al. simulated AlSi10Mg laser melting using a gaussian heat source programmed in ANSYS APDL [13]. In a separate effort, Liu et al. developed a 3D

microscale FE model to analyze temperature evolution and material bonding in a porous powder bed. Powders were modeled as layered cubic structures and were exposed to a gaussian heat source [14]. Each of these simulations provides valuable insight on the development of transient thermal finite element models that simulate a changing laser source applied to a powder bed. Most of the models considered temperature and phase dependent material properties to capture the material changes that occur during the build process. Despite the success of these models, the melting and solidification process does not reflect the scale or solid-state diffusion mechanisms present in the μ-SLS system. Copper particles in the μ-SLS system do not form a melt pool. Instead, they undergo particle-particle diffusion below the melting temperature. This fundamental sintering mechanism must be considered when predicting thermal evolution and resulting part shapes for the μ-SLS system.

1.3 Laser Sintering Models Using Metal Nanoparticles

Yang et al. modeled a copper nanoparticle low temperature sintering process using simple geometry and a temperature dependent thermal conductivity that quickly ramps up to bulk conductivity at high temperatures. This model implements a moving gaussian heat source to estimate a moving laser spot and measures the temperature evolution during laser motion [15]. Zacharatos et al. modeled a selective laser sintering process using silver nanoparticles as the powder material. This model also predicted thermal evolution in the metal powder bed by incorporating a moving gaussian beam [16]. While both [15] and [16] adjusted the thermal conductivity as functions of temperature, neither simulation modeled thermal conductivity as a function of densification. While thermal conductivity is a function of temperature, the primary contributor to elevated thermal conductivity during sintering is the increase in densification and neck formation between adjacent nanoparticles. Therefore, a model that accounts for this densification process is closer to the fundamental physics that drives microscale laser sintering. Additionally, the moving laser beam differs considerably from the stationary, mask-based selectivity present in the μ-SLS system. The bed-scale model developed in this work addresses these concerns when predicting thermal evolution and part formation in the nanoparticle powder bed. Additionally, this thermal model will integrate into an iterative control framework used to optimize the μ-SLS system parameters and improve the feature resolution of printed parts.

2. Methodology

2.1 Model Overview

The bed-scale FE model developed in this work solves the heat equation shown in Equation 1 to estimate the full transient evolution of the temperature field present within the μ-SLS powder bed in response to laser heating. Results from nanoparticle models developed in previous work estimate the effective property relationships between the temperature, density, and thermal conductivity of small packings of metal nanoparticles within the particle bed [17, 18]. These

property relationships are incorporated into the bed-scale model to accurately simulate the evolving particle morphology that occurs within the particle bed during sintering. As a result, the bed scale model can produce accurate temperature predictions using a simplified geometric model of the particle bed.

2.2 Model Geometry

The bed-scale model simulates a thin copper particle layer (.0012mm in thickness) resting on a thick glass substrate (1mm in thickness). The thin copper bed is split into two regions: a rectangular inner mesh region in the immediate vicinity of the laser mask (sized at 1.5mm x 3mm), and an outer rectangular meshing region (sized at 4mm x 6mm) that surrounds the inner region. These two copper regions are the same thickness, sit at the same z-location and are in perfect thermal contact with each other. The inner region is used for analysis of heat spread and degree of simulated sintering while the outer region is used to decouple boundary effects from the resulting temperature distribution. The split regions allow for accurate modeling of the powder bed while maintaining a reasonable computation time. Each copper rectangle is designed to be as simple as possible to minimize computation time. In the true system, the powder bed is composed of many nanoparticles whose properties evolve as functions of temperature and degree of densification. To account for this geometric discrepancy between the system and simulation, each element in the FE mesh has temperature and density dependent thermal properties that update throughout the simulation. The full model geometry is shown in Figure 1, and the coper meshing regions are shown in Figure 2.

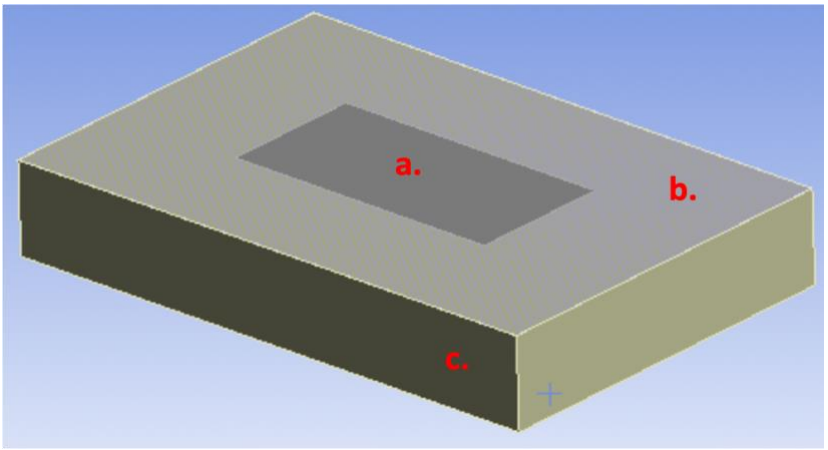

Figure 1: Physical geometry used in FEA simulations, with (a) representing the inner copper region (fine mesh), (b) representing the outer copper region (coarse mesh), and (c) representing the glass substrate

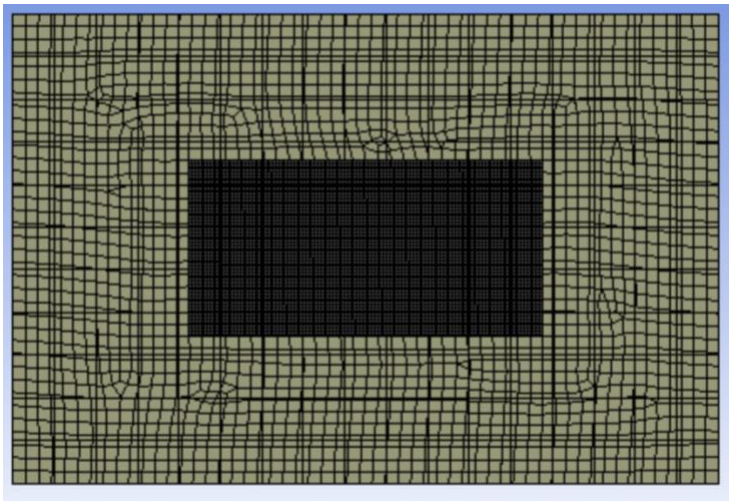

Figure 2: Copper Meshing Regions (inner fine mesh and outer coarse mesh)

2.3 Modeling Properties and Settings

The transient thermal model simulates a full 2 second sintering window and can extend or reduce this window if needed. This model uses ANSYS defined defaults for its time stepping settings, with 2 seconds of sintering corresponding to 133 sintering timesteps of various sizes depending on the applied heat load. As discussed, the FE model is also integrated with property curves that model the evolution of thermal properties within the powder bed as the morphology of the particles change during sintering. Values for density and thermal conductivity for each element are updated at 10 specified timesteps over the 2 second simulation window (every 0.2 seconds of simulation time) based on the element temperatures at the given timesteps. These special timesteps, referred to as loadsteps, allow the simulation to pause briefly during the simulation runtime. During the pause, the simulation exports the temperature and location of each Finite Element, in addition to the elapsed sintering time. Files containing this information are then imported into a MATLAB script (executed by an ANSYS system command). The MATLAB script performs several tasks during runtime. First, it determines which elements are sintering by comparing the element temperatures to the 450 °C copper sintering threshold. Elements labeled as “sintering” are then passed to the property update portion of the script. At this step, sintering elements have their density and thermal conductivity updated according to property relationships developed in the nanoparticle models discussed in [17, 18]. Element temperature and sintering time are used with densification curves to determine the density change occurring for each sintering element. This density value is then used to estimate the new thermal conductivity of the element. Finally, the script stores information regarding the properties and sintering status of each element before it completes its run. At script completion, the ANSYS Transient Thermal simulation imports the new properties for each element, applies them to the system, and continues the simulation process at the next timestep. This process repeats at each of the specified loadsteps. ANSYS APDL scripts inserted into the model are used to control the entire property update process. A summary of the bed-scale modeling workflow is shown in Figure 3.

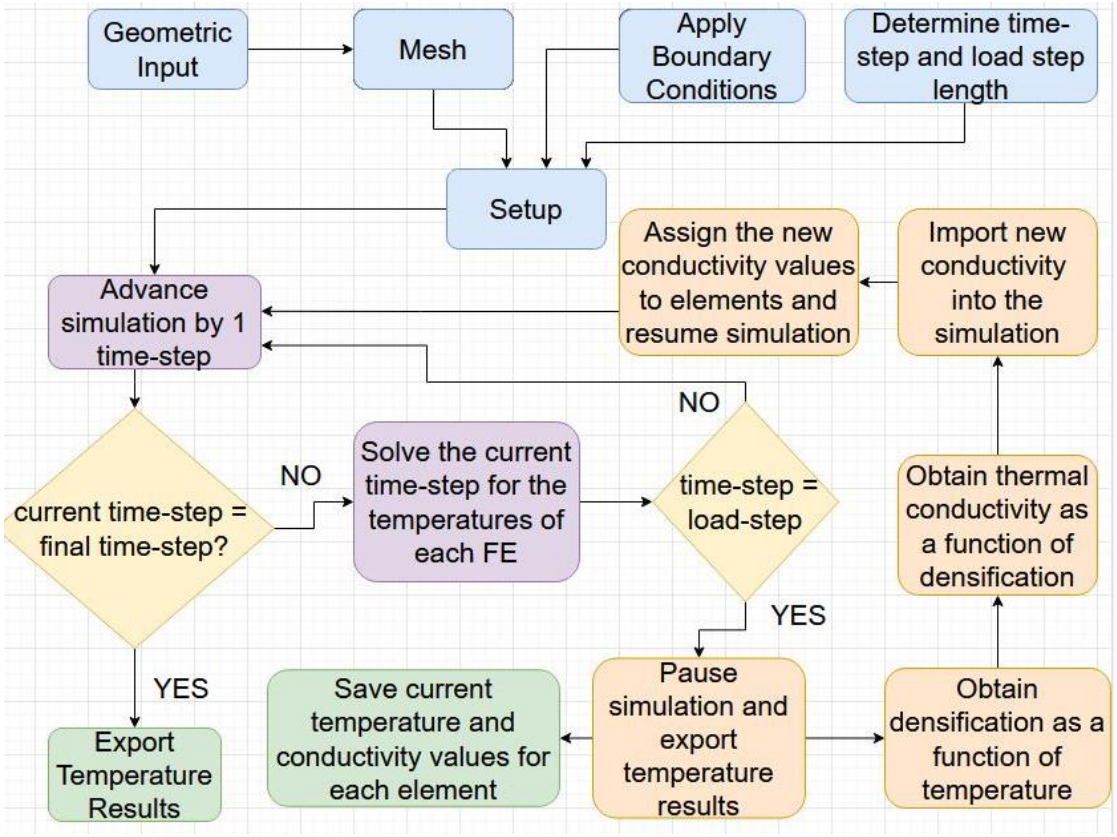

Figure 3: Full Part-Scale Modelling Workflow

The current simulation updates the thermal properties every 0.2 seconds of simulation time. This coarse property update frequency helps improve computation time at the cost of sudden, larger property changes that result in sudden redistributions of temperature. The final version of this model will update with a much finer frequency to improve accuracy of the temperature results.

2.4 Boundary Conditions

The initial density and conductivity are set to the values determined by the nanoparticle models (2600 kg/m^3 and 1 W/m*k). These properties are updated at each loadstep of the simulation. The FE simulation is initialized at room temperature, with all elements set to 22 °C at timestep 0. The bottom of the glass block is held at 22 °C for the duration of the simulation, and all other faces in the model are insulated. Convection and radiation are not considered in the FE model, as the contributions to both are negligible when compared to heat conduction at the microscale. Contributions of convection and radiation were tested empirically during model development and found to have less than a 1% impact on the final results at significant computational cost.

Heat sources used in the μ-SLS system can take the form of any shape and can change many times over the course of a 2 second sintering window. A Digital Micromirror Device (DMD) is used to control the laser power distribution applied to the copper powder bed. The DMD and the upstream fly-eye lens used in the μ-SLS optical system allow the laser to split into a grid of uniform laser beams. The DMD uses a digital binary/grayscale mask to control which portions of the distributed laser energy are passed through to the substrate. White pixels in the digital mask transmit the maximum laser power at the corresponding location, while black pixels restrict all laser power transmission. Gray values in between white and black pixels transmit laser power between 0 and the maximum irradiance based on the specific pixel color. Laser irradiation passing through the DMD mask passes through a downstream optical system before exposing the copper bed. The 1920x1080 pixel binary image can expose a 2.3 mm x 1.3 mm region when all pixels are white. An example binary mask is shown in Figure 4.

Figure 4: Simple "double-I" Binary Mask (1920x1080 Pixel Count) used to control DMD mirrors and selective application of laser power

The bed scale model does not use manually applied heat sources to simulate mask driven laser power application. The regions of laser power application can take the form of any pixelated grayscale image, and these images can change many times during simulation. Instead, APDL scripts are used to apply laser power directly to specified elements during the specified loadstep update process. When the simulation pauses and calls the MATLAB script, element locations are used to determine the position of each element relative to the regions exposed to laser irradiation by the current digital mask. Elements residing under white pixels are exposed to the maximum value of laser irradiation, while elements residing under black pixels are not exposed to laser irradiation. Masks can change to a completely different mask at any of the specified loadsteps. Elements that experience laser radiation have a heat generation term applied to them, with a maximum possible intensity value of 15800 W/cm^2. In summary, at each specified loadstep, heat generation values and material properties are specified for each element in the system based on the

element's temperature, time under sintering conditions, and location relative to the applied laser mask.

Since the bed scale thermal model tracks density as a function of temperature and sintering time, the densification of all elements in the system is known at the end of the simulation. These density values in addition to the sizes of each element, can be used to reconstruct a simulated sintered part. This sintered part can be visualized in 2D and in 3D.

3. Results and Experimental Validation

3.1 Model Results

Results from the bed-scale model are displayed as 2D profiles despite the model solving a full 3D simulation of copper on glass. The temperature gradients along the z-axis (thickness direction) are very small, so averaged temperatures along the thickness direction are very similar to the viewable surface temperatures. Simulations were performed for many input masks over a 2 second sintering window. Throughout each simulation, intermediate density predictions were performed using available temperature data for all elements in the mesh. Example temperature results from these simulations, along with their corresponding input mask (constant mask vector) and predicted part densities are shown in Figure 5.

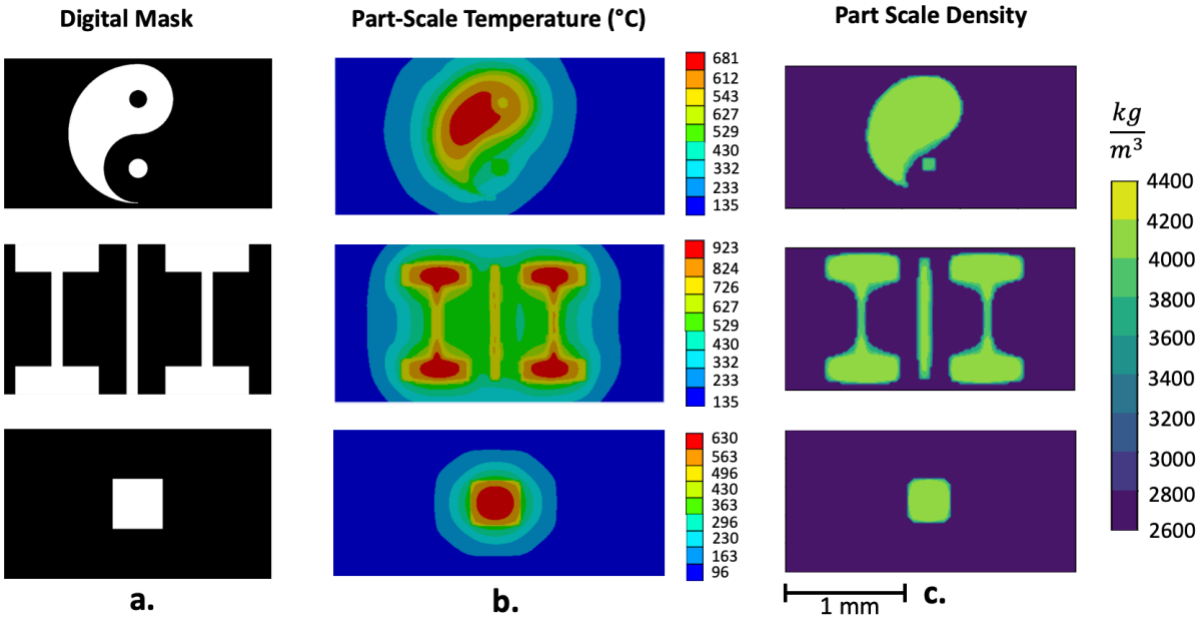

Figure 5: Sample Part-Scale Modeling Results When Bed is Exposed to Different Laser power Distributions. (a). 3 sample binary masks used to control laser power distribution for simulated heat transfer, (b). simulated thermal profiles given selective heat application over a 2 second sintering window, (c). resulting part shapes obtained through property update process during 2 second thermal simulation

The results in Figure 5 show the final temperature profiles and part shapes predicted by the bed-scale model. The shapes of the temperature profiles are dominated by the shape of the input laser mask, although particle-particle conduction within the bed results in curved isotherms and part edges. This is best illustrated by the "double-I" mask on the second row of Figure 5, where the resulting part has overextended edges and filleted corners that indicate unwanted heat conduction in regions beyond the target part shape. These heat affected zones prevent the production of small scale parts with resolutions on the order of a single micrometer. The temperatures present in these results are higher than those present in the physical μ-SLS system due to the elevated laser powers used in the model. A small reduction of the chosen laser power will alleviate some of the excess sintering present in the results, but the curved temperature contours and part edges will remain given the radial nature of heat conduction from a laser spot.

The transient evolution of temperature and part densification for a single mask is shown in Figure 6, and the temperature at specified elements are shown over time in Figure 7.

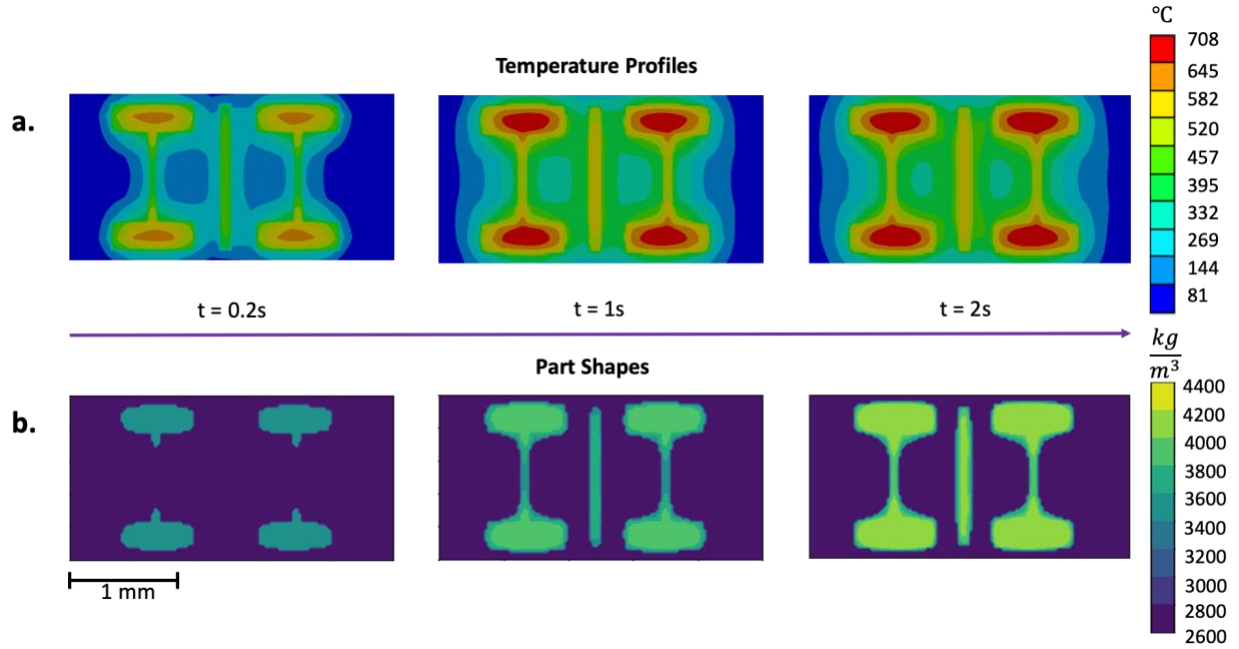

Figure 6: (a). Temperature profiles at 3 timesteps during the laser sintering process for a given input mask. (b). Predicted single-layer part shapes at 3 specified timesteps during sintering using the same digital mask

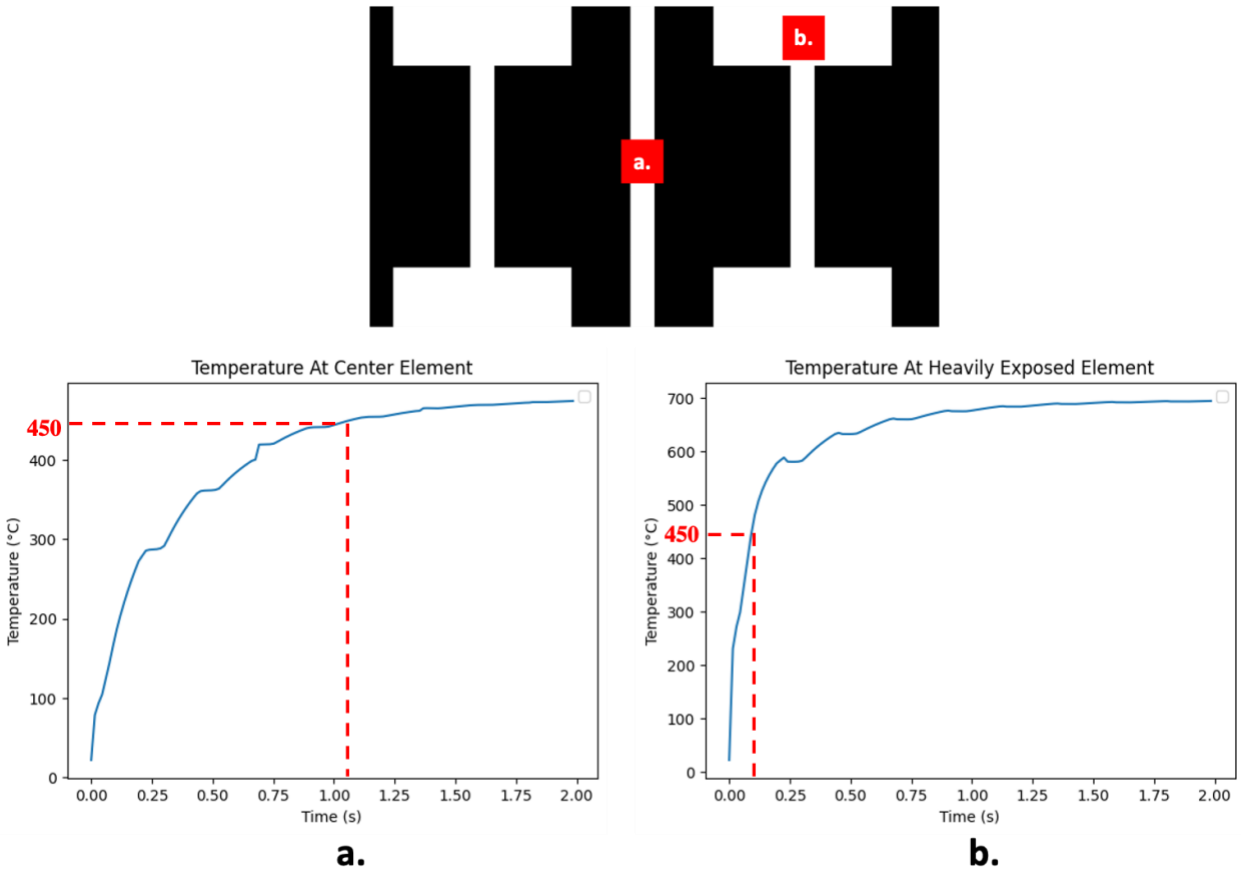

Figure 7: Single element temperature plots over time for the full 3s sintering window (a). for an element at the center of the "double-I" binary mask exposure region, and (b.) for an element in a region of dense laser exposure

The results shown in Figure 6 and Figure 7 illustrate the rapid initial rise in temperature experienced by the nanoparticle bed during the sintering process. Temperatures in the μ-SLS system typically reach equilibrium above the sintering threshold in less than 1 second, however densification occurs over a longer time window after the sintering temperature is reached. Figure 7 shows that the elements exposed to higher concentrations of laser power can reach elevated temperatures in less than half a second, with sintering taking additional time in regions with reduced laser exposure. Additionally, temperatures are updated more frequently than density and thermal conductivity values for all elements during simulation. This results in sudden, discrete updates to the density values of each sintering element when these properties ae modified. These sudden changes produce the jagged temperature plots in Figure 7, where sudden property updates cause a rapid redistribution of temperature in the system. Increasing the frequency of these property update loadsteps will result in a reduced time difference between property changes and smoother temperature profiles over time.

3.2 Experimental Validation

Initial validation of the bed scale thermal model has been performed by comparing laser sintered experimental results with simulation results. A simple square mask and a simple rectangular mask were used for initial validation. The rectangular mask corresponds to the "Full-On" state of the DMD, where all possible pixels are white. These masks are shown in Figure 8.

Figure 8: Binary Digital Masks Used for Simulation Validation. (a). 1080 x 1080 pixel square mask. (b). 1920 x 1080 pixel rectangular mask. Full DMD (all pixels are on)

Sintering experiments were performed using the same binary image masks used as simulation input. Sintering experiments were performed originally using the square mask shown in Figure 8a at maximum laser power (935 W). This original sintering experiment was run for 3 seconds with constant laser power and a constant mask. Optical images were taken using an optical profilometer microscope. These images were sized using image processing software.

Once the preliminary experiment was performed, the bed-scale finite element simulation was run as a comparison using default parameters. Due to the particle scale and the evolving nanoparticle morphology, the exact absorptivity at varying degrees of sintering are currently not exactly known. Other properties such as density and thermal conductivity are estimated using the simulations discussed previously, and the ambient conditions are known. To account for the uncertain absorptivity value, the finite element simulation was run with several values of absorptivity between 0.005 and 0.02, and the absorptivity that best matched the results was chosen (0.01). The final simulated result and the corresponding sintering experiment is shown in Figure 9.

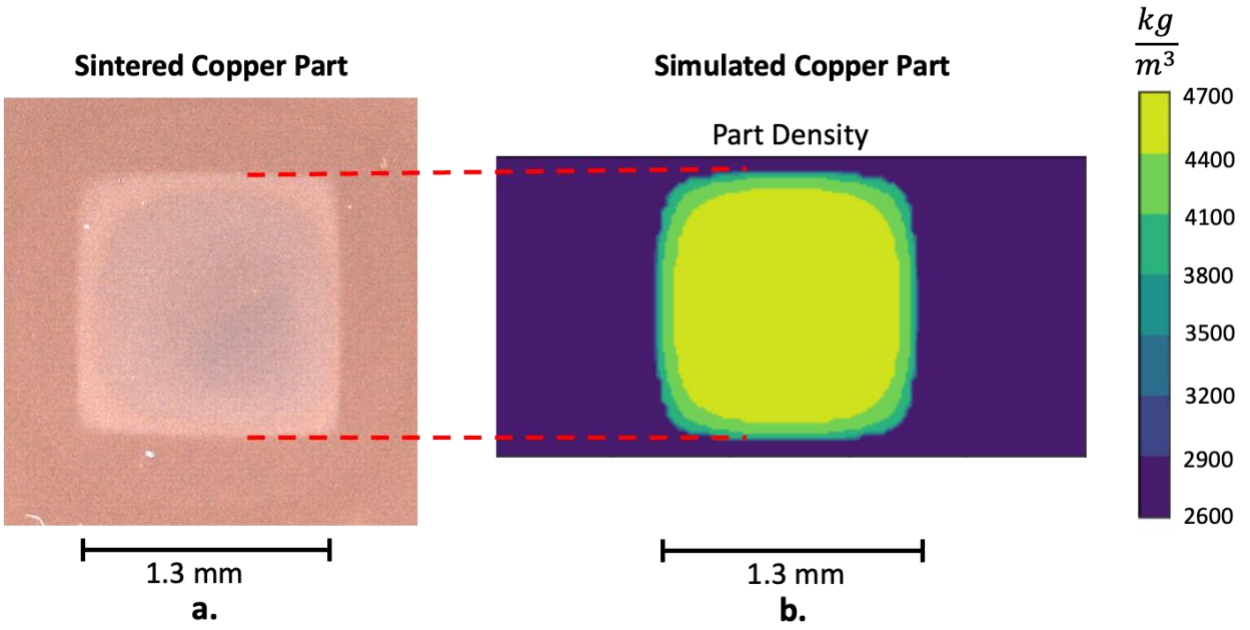

Figure 9: Comparison between sintered square (a) and simulated sintered square (b). Both squares are roughly the same major dimensions, although the simulated square is a bit smoother near the edges

Once the simulations were lightly calibrated with sintering experiments, additional sintering experiments were performed, and the resulting parts were compared with part size estimates from the bed scale sintering model. Experiments were performed at the following laser powers for the square mask: 935 W, 810 W, and 560 W. A single experiment at 935 W was performed for the "full on" mask. Simulations with the same sintering duration and input laser mask were also performed. All sintering simulations were performed on an approximately 1-1.2 mm thick copper-ink powder bed. The resulting simulated vs sintered parts are shown in Figure 10.

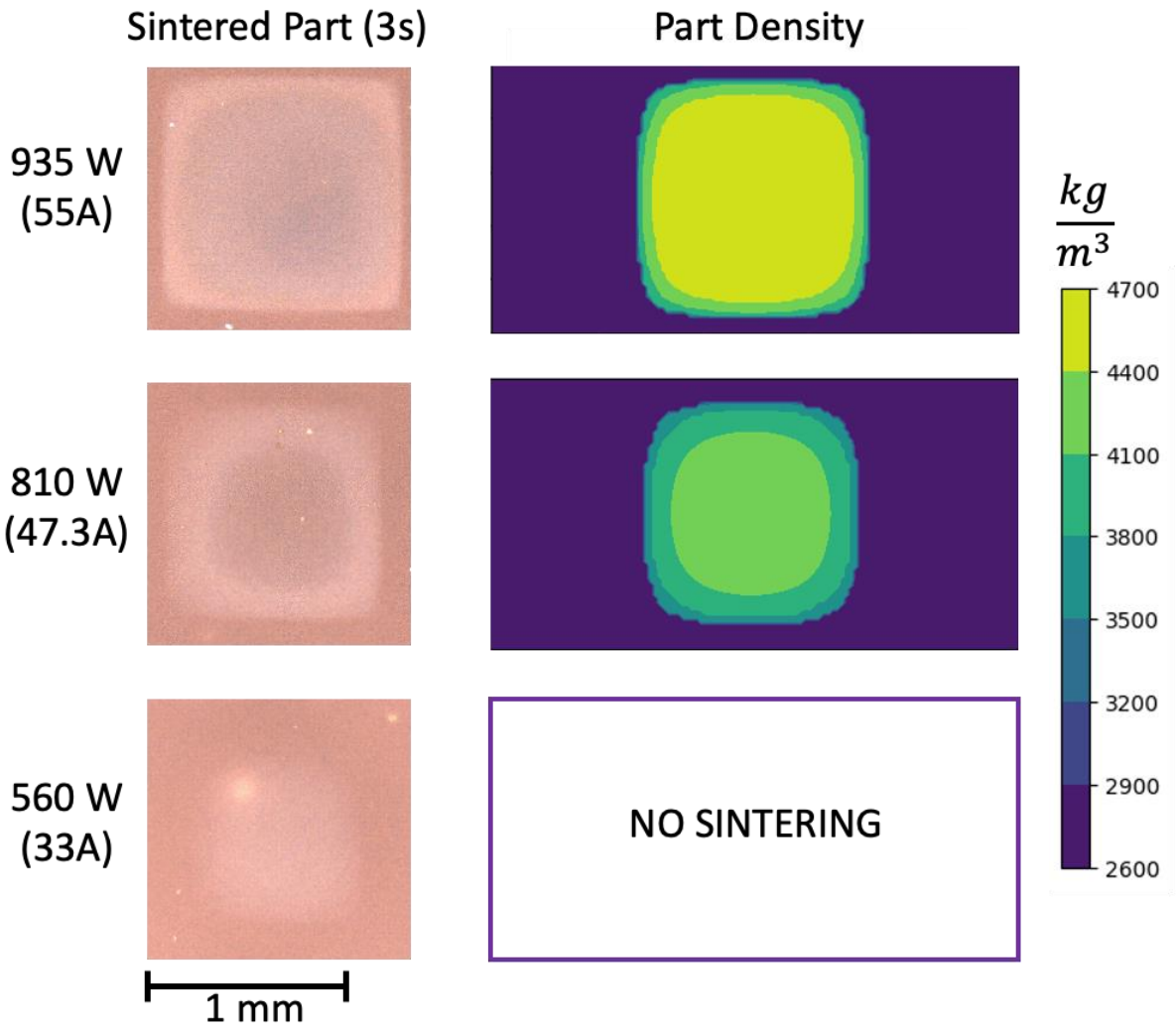

Figure 10: Sintered vs Simulated Part Comparison (Varying Powers). Experiments and simulations performed for 935 W, 810 W and 560 W laser powers using a 300 burst count (BC) duration. Laser powers adjusted in simulation to match experimental laser power

The simulated results agree well with the sintering experiments, as the part shapes nearly match for the 935 W and 810 W experiments. The light sintering present in the 560 W experiment was not captured by the simulation, although the predicted temperatures fell just below the sintering threshold indicating reasonable accuracy. Additionally, the max temperatures for each simulated part fall in between the sintering threshold of 450 °C and the melting temperature of 1085 °C. Given that sintering experiments generally reach maximum temperatures in the 550-650 °C range, the simulated maximum temperatures seem to overestimate the temperature rise in the particle bed.

A final preliminary experiment was performed with the "Full-On" mask shown in Figure 8. The simulated comparison is shown in Figure 11.

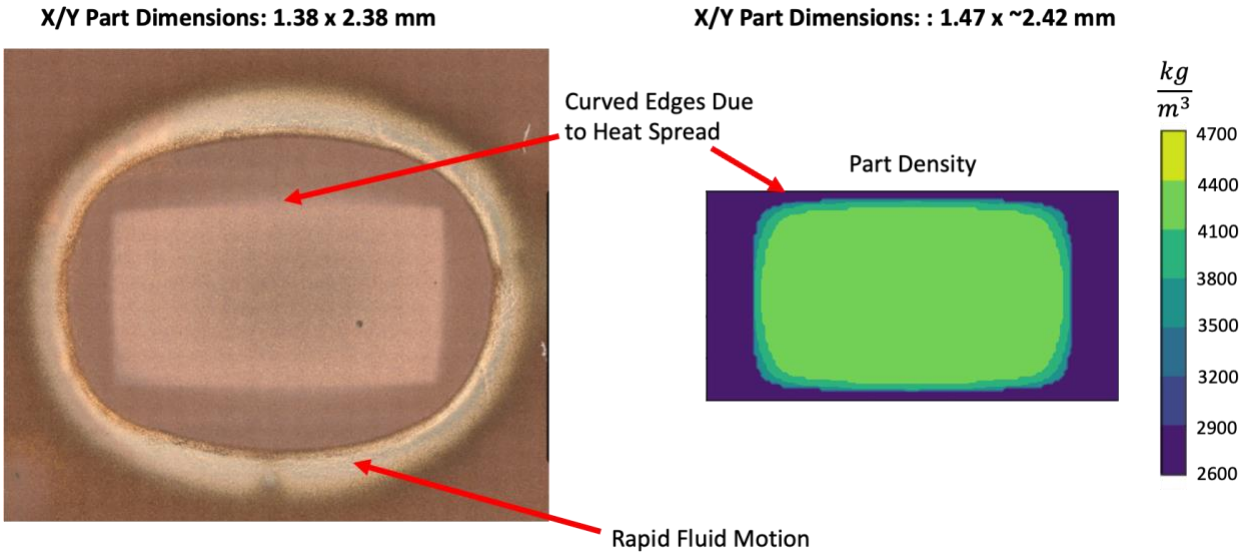

Figure 11: Sintered vs Simulated Sintered Part Using Full Laser Mask

The simulation accuracy from the experiment shown in Figure 11 is somewhat lower than the comparisons shown in Figure 1-. The thermal simulation captures the general size and shape of the slightly curved rectangular part, but the simulated corners show more curvature. Additional copper sintering experiments to identify the exact sintered region must be performed before iterative simulation adjustments can be made to more accurately model part formation for various masks. Figure 11 also depicts an outer ring surrounding the sintered part. This ring forms as the result of rapid fluid motion during sintering. This rapid motion should not greatly impact the sintering process, especially when samples are properly dried before sintering.

4. Limitations and Future Work

4.1 Improved Characterization of Copper Sintering

The bed-scale simulation accuracy is currently limited by knowledge gaps in copper sintering characterization. While optical images give good information about the regions that undergo sintering, the exact boundary between sintered and unsintered part is not known with high certainty for copper parts. The sintered part optical images shown in Figure 10 and Figure 11 contain multiple identifiable color regions. The 935 W sintered image contains three of these regions: a region along the outer border of the image that is known with high certainty to contain unsintered nanoparticle ink outside of the sintering part. However, the part itself contains both a lighter and darker region. The lighter region is used in this work as the "sintered part" for modeling validation, while the exact cause of the darker region is somewhat unknown. SEM imaging results have shown both the lighter and darker regions to contain sintered nanoparticles, but a full mapping of the entire part using SEM images on the order of .1-1 micrometers in length is prohibitively time intensive, and nanoparticle SEM images are difficult to identify by visual inspection. These

limitations will be addressed by the development of a more robust part characterization technique employing SEM imaging and a Convolutional Neural Network based regression model capable of identifying the degree of densification in an SEM image. This will be combined with an efficient layout of imaging points across the sintered part to identify the sintered region with high certainty.

4.2 Quantify Incident Laser Power and Absorptivity of Particle Bed

The bed-scale FE model currently uses an absorptivity value of 0.01 and an incident laser heat flux of 1.58×10^8 W/m^2. The laser flux is derived from previous experimental work but is likely outdated given changes to the system and degradation of the equipment. The absorptivity value however is solely derived from calibration between copper sintering results and simulated part shapes. Experimental measurements are available to better quantify these simulation variables. First, laser intensity can be directly measured downstream of the focusing optics using a power meter. The power meter would measure incident laser power at various values for input current. This laser power should match the laser power incident on the copper powder bed during sintering. Although the power meter would quantify incident laser power, only a fraction of that power would be absorbed by the thin copper powder bed. At roughly 1 micron in thickness, the copper powder bed will likely transmit a considerable portion of the incident laser energy. The bed-scale model requires both the incident laser power and a measured absorptivity to determine the heat generation at each element in the system. Measurement of the effective absorptivity of the copper powder bed will be performed using the Cary 5000 UV/VIS NIR system. Unsintered and oven sintered samples will be placed in the UV/VIS system where the fraction of reflected and transmitted radiation will be measured. Given that these values sum with absorptivity to equal 1, the effective absorptivity of the copper bed can be directly calculated from the results.

4.3 Mesh Refinement and Controls Integration

The bed-scale model is also currently using a limited mesh size to perform quick calculations during model development. The final version of the model will need to undergo a robust mesh refinement procedure to eliminate additional uncertainty due to the coarse mesh. The existing model uses a 60x118x1 grid mesh for the inner copper region. The x-y mesh grid will be reduced and tested iteratively as part of a mesh refinement procedure to test for mesh convergence. This refinement process will also include the addition of a swept mesh in the thickness direction for improved.

Finally, a control framework with an objective function defined by the heat conduction equation (Equation 1) is currently under development. This control framework is designed to determine the laser power for each timestep at every pixel in the DMD independently using the temperature predictions from a transient thermal model. The thermal model is used to predict the temperature evolution at subsequent timesteps. At each optimization timestep, the control algorithm employs the thermal model to predict the temperature distribution a few timesteps into

the future using the current mask, and then adjusts the laser mask based on error between the predicted temperature distribution and the ideal distribution. The thermal model then returns to the optimization timestep and continues the simulation with the new mask. The controller will ensure sufficiently high temperatures for sintering at the required locations while keeping temperatures sufficiently low elsewhere to avoid unwanted sintering and minimize the heat affected zones.

5. Conclusions

This work develops a bed-scale model capable of predicting the transient thermal evolution and part densification processes that occur during part builds using the μ-SLS system. The model produces 3D temperature predictions at every timestep over a variable sintering window. At various specified timesteps throughout the simulation, these temperature values are used as inputs to temperature dependent property relationships for element density and thermal conductivity. These new thermal properties are returned to the FE model for subsequent timestep processing. The results of this modeling produce thermal profiles and predicted part shapes for a given input mask. Results show good agreement with simple parts sintered using the μ-SLS system. Predicted parts show curved edges and rounder corners indicative of the excess heat conduction and unwanted HAZ formation that limits the minimum achievable part resolutions present in the real system. Further validation with more complex part shapes and better sintered part characterization will improve modeling accuracy. Ultimately, this bed-scale model will be integrated into a digital mask optimization framework to preemptively optimize the shapes of parts printed using the μ-SLS system.

Acknowledgements
This paper contributes to work supported by the National Science Foundation under Grant No. 2141044

References

[1] Govett, T., Kim, K., Lundin, M., and Pinero, D., 2012, "Design Rules for Selective Laser Sintering," Mechanical Engineering Design Projects Program, The University of Texas, Austin, TX, accessed Oct. 19, 2018, https://www.me.utexas.edu/~ppmdlab/files/designers.guide.sls.pdf.

[2] Sager, B., Rosen, D., 2002, "Stereolithography Process Resolution," Georgia Institute of Technology, Atlanta, GA.

[3] Roy, N.K., Behera, D., Dibua, O. G., Foong, C. S., Cullinan, M., 2019, "A novel microscale selective laser sintering (μ- SLS) process for the fabrication of microelectronic parts," *Microsystems and Nanoengineering*, 64. https://doi.org/10.1038/s41378-019-0116-8.

[4] Roy, N. K., Foong, C. S., Cullinan, M. A., 2016, "Design of a Micro-scale Selective Laser Sintering System," 2016 Annual International Solid Freeform Fabrication Symposium.

[5] Roy, N., Yuksel, A., Cullinan, M., "Design and Modeling of a Microscale Selective Laser Sintering System," 2016, ASME 2016 11th International Manufacturing Science and Engineering Conference.

[6] Roy, N., Dibua, O., Foong, C. S., Cullinan, M., 2017, "Preliminary Results on the Fabrication of Interconnect Structures Using Microscale Selective Laser Sintering", Proceedings of the ASME International Technical Conference and Exhibition on Packaging and Integration of Electronic and Photonic Microsystems.

[7] Nelson, C., McAlea, K., Gray, D., 1995, "Improvements in SLS Part Accuracy, Annual International Solid Freeform Fabrication Symposium," pp 159-169.

[8] Foroozmehr, A., Badrossamay, M., Foroozmehr, E., Golabi, S., Finite Element Simulation of Selective Laser Melting process considering Optical Penetration Depth of laser in powder bed, Materials & Design, 89 (2016), 255-263, https://doi.org/10.1016/j.matdes.2015.10.002

[9] Bruna-Rosso, C., Demir, A. G., Previtali, B., Selective laser melting finite element modeling: Validation with high-speed imaging and lack of fusion defects prediction, Materials and Design, 156 (2018), 143-153, https://doi.org/10.1016/j.matdes.2018.06.037

[10] Huang, Y., Yang, L.J., Du, X.Z., Yang, Y.P., Finite element analysis of thermal behavior of metal powder during selective laser melting, International Journal of Thermal Sciences, 104 (2016), 146-157, https://doi.org/10.1016/j.ijthermalsci.2016.01.007

[11] Lee, K.H., Yun, G. J., Temperature thread multiscale finite element simulation of selective laser melting for the evaluation of process, Advances in Aircraft and Spacecraft Science, 8 (2021), https://doi.org/10.12989/aas.2021.8.1.000

[12] Fu, C.H., Guo, Y.B., 3-Dimensional Finite Element Modeling of Selective Laser Melting Ti-6Al-4V Alloy, 2014 International Solid Freeform Fabrication Symposium

[13] Liu, S., Zhu, H., Peng, G., Yin, J., Zen, X., Microstructure prediction of selective laser melting AlSi10Mg using finite element analysis, Materials & Design, 142 (2018), 319-328, https://doi.org/10.1016/j.matdes.2018.01.022

[14] Liu, F.R, Zhang, Q., Zhou, W.P., Zhao, J.J., Chen, J.M., Micro scale 3D FEM simulation on thermal evolution within the porous structure in selective laser sintering, Journal of Materials Processing Technology, 212 (2012), 2058-2065, https://doi.org/10.1016/j.jmatprotec.2012.05.010.

[15] Yang, G., Xu, G., Li, Q., Zeng, Y., Zhang, Y., Hao, M., Cui, C., Understanding the sintering and heat dissipation behaviours of Cu nanoparticles during low-temperature selective laser sintering process on flexible substrates, Journal of Physics D: Applied Physics, 54 (2021), https://doi.org/10.1088/1361-6463/ac0d73

[16] Zacharatos, F., Theodorakos, I., Karvounis, P., Tuohy, S., Braz, N., Melamed, S., Kabla, A., De la Vega, F., Andritsos, Hatziapostolou, A., Karnakis, D., Zergioti, I., Selective Laser Sintering of Laser Printed Ag Nanoparticle Micropatterns at High Repetition Rates, Materials, 11, (2018), 2142, https://doi.org/10.3390/ma11112142

[17] Dibua, O., Yuksel, A., Roy, N., Foong, C.S., and Cullinan, M., 2018, "Nanoparticle Sintering Model, Simulation and Calibration Against Experimental Data," Journal of Micro and Nanomanufacturing, 6, 041004. https://doi.org/10.1115/1.4041668

[18] Grose, J., Dibua, O.G., Behera, D., Foong, C.S., Cullinan, M., Simulation and Property Characterization of Nanoparticle Thermal Conductivity for a Microscale Selective Laser Sintering System, J. Heat and Mass Transfer, 145 (2023), https://doi.org/10.1115/1.4055820